Impact of surface inhomogeneity on solar radiative transfer under overcast conditions

Zhanqing Li[1]
Department of Meteorology, University of Maryland, College Park, Maryland, USA

Maureen C. Cribb
Earth System Science Interdisciplinary Center, University of Maryland, College Park, Maryland, USA

Alexander P. Trishchenko
Canada Centre for Remote Sensing, Ottawa, Ontario, Canada

Received 20 June 2001; revised 26 November 2001; accepted 18 January 2002; published 24 August 2002.

[1] The goal of this study was to assess the ability of the Moderate-Resolution Transmittance 4 (MODTRAN-4) code to simulate high-resolution shortwave (SW) fluxes given detailed and complete input information under overcast conditions. The study underlines the impact of surface inhomogeneity on the closure of SW radiative transfer. It also leads to a method of estimating surface spectral areal-mean albedo from downwelling solar transmittance measurements. The investigation made use of ample Atmospheric Radiation Measurement (ARM) field data collected by a suite of instruments, including broadband and narrowband radiometers and spectrometers, cloud radar and lidar, microwave radiometer, atmospheric sounding instruments, and satellite data. Furnishing the MODTRAN-4 code with observed atmospheric, cloud, and surface parameters generates spectral solar transmittance at the surface and reflectance at the top of the atmosphere (TOA). The transmittances were compared with the Rotating Shadowband Spectroradiometer measurements and showed significant discrepancies in the near-infrared (NIR) region, the bulk of which was attributed to the use of unrepresentative surface spectral albedos. A field campaign was undertaken to collect surface albedo data for a wide variety of land cover types near the ARM Central Facility. The sampled data were combined with thematic mapper/Landsat-based land cover classification data to map surface spectral albedo. Substitution of the derived areal-mean spectral albedo into the MODTRAN-4 model eliminates major discrepancies in the NIR, and also leads to good agreements with surface solar broadband fluxes and TOA satellite spectral reflectance. On the basis of these findings, one may use downwelling spectral transmittance data, together with detailed cloud and atmospheric information, to estimate surface effective areal-mean albedo. The estimated values agree well with those derived from the ground survey data. Following the method, a data set of effective areal-mean spectral albedo throughout a year was obtained. *INDEX TERMS:* 0320 Atmospheric Composition and Structure: Cloud physics and chemistry; 3360 Meteorology and Atmospheric Dynamics: Remote sensing; 1640 Global Change: Remote sensing; 3359 Meteorology and Atmospheric Dynamics: Radiative processes; 3322 Meteorology and Atmospheric Dynamics: Land/atmosphere interactions; *KEYWORDS:* radiation, radiative transfer, surface albedo, inhomogeneity, remote sensing, ARM

1. Introduction

[2] Solar radiative heating is the primary driving force of atmospheric and oceanic movements. Variable radiative heating/cooling in the atmospheric column drives vertical atmospheric convection and global general atmospheric and oceanic circulations are the primary responses to the uneven distribution of radiation. Modeling Earth's weather and climate and the changes incurred by any external or internal forcings thus requires a good knowledge and understanding of the disposition and distribution of solar radiation, which is unfortunately still fraught with large uncertainties [*Wild et al.*, 1995; *Li et al.*, 1997; *Arking*, 1999]. The breakdown of solar energy in the atmosphere and at the surface can be computed by radiative transfer models founded on the classical electromagnetic and quantum mechanics theories. While the fundamentals of radiative transfer theories are well-established, radiative transfer models used to describe

[1]Also at Earth System Science Interdisciplinary Center, University of Maryland, College Park, Maryland, USA.

0148-0227/02/2001JD000976$09.00

radiative processes in the real world are complex and difficult due partly to a lack or incomplete knowledge of a large number of radiatively sensitive variables of multiple numbers of freedom and dimensions that act on a wide range of scales [*Wielicki et al.*, 1995; *Rossow et al.*, 2002], and uncertainties in the spectroscopic data bases [*Giver et al.*, 2000]. The problem is further complicated by, among other things, the ubiquitous three-dimensional (3-D) cloud morphology, uncertain cloud microphysics, and the inhomogeneous surface boundary.

[3] The complex nature of the problem often makes the seemingly straightforward task of testing the closure of radiative quantities cumbersome and challenging [*Trishchenko et al.*, 2001]. Even for ideal cases of overcast cloudy conditions, controversial findings have emerged from time to time. *Stephens and Tsay* [1990] reviewed various studies on discrepancies found between observed and modeled atmospheric/cloud solar absorption. In general, there appeared to be more discrepancies in the near-infrared (NIR) region than at other wavelengths. Given the inadequacy of some previous observational techniques, they called for a greater effort at improving the accuracy of observations. Unfortunately, substantial differences still exist among more recent measurements made simultaneously with different instruments in a field campaign named the Atmospheric Radiation Measurement (ARM) Enhanced Shortwave Experiment (ARESE) [*Li et al.*, 1999; *O'Hirok et al.*, 2000]. In addition, a major source of uncertainties lies in the synergy between measurements made below and above a cloud layer [*Marshak et al.*, 1999], and the effects of cloud inhomogeneity on the determination of net fluxes [*Barker and Li*, 1997]. To tackle these problems, the U.S. Department of Energy sponsored a second ARESE field experiment conducted in the South Great Plain (SGP) in Oklahoma in the spring of 2000. Preliminary analyses of the data revealed no evidence of substantial discrepancies between modeling and observations of bulk solar radiative quantities but still some differences were found in the NIR region [*Ellingson*, 2001]. No sound explanation has been found to account for this spectral discrepancy.

[4] It is a rather complex problem to model solar radiative transfer in a cloudy atmosphere. Numerous input data are needed to define a closed problem: atmospheric profiles of humidity and liquid water, temperature and pressure, cloud boundaries and cloud microphysics, concentration and optical properties of aerosol, let alone the complex 3-D cloud morphology. As a result, attributing a discrepancy in the output to any of the input variables requires a painstaking investigation into each of the contributing factors. So far, much attention has been focused on atmospheric and cloud variables. The influence of the surface boundary condition on radiative transfer has not been carefully investigated, especially in dealing with atmospheric and cloud absorption issues. The significance of surface albedo on radiation modeling for bright snow/ice-covered surfaces has been recognized for a long time [*Pyatnenkov*, 1959; *Gardiner*, 1987], whereas much less attention has been given to vegetated surfaces. While vegetated surfaces look dark in the visible band with an albedo typically $\sim$5%, it is very bright in the NIR part of spectrum where the magnitude of the albedo can reach as high as 60–70% or more. Such a strong contrast was employed to infer cloud optical depth [*Marshak et al.*, 2000] by virtue of multiple reflections between the surface and the cloud. Except for large uniform areas of forest and savanna, land surface is usually quite inhomogeneous. This is especially the case over ARM's SGP locale where a variety of land cover types of small scale (mostly different types of crops) exist. Multiple reflections between the surface and the cloud layer lead to radiative mixing of local reflectances at a distance comparable to cloud height thus providing a strong coupling between downward radiation and surface albedo. Point-wise measurements of surface albedo may only represent very small areas; on the other hand, ground-based observations of downwelling irradiance under cloudy conditions are modulated by photon exchange between the surface and clouds over a much larger area.

[5] In light of the interaction between radiation and the surface boundary, special care needs to be exercised in the interpretation of comparisons between modeled and observed spectral fluxes. This study demonstrates the impact of surface inhomogeneity on the solar radiative transfer under cloudy skies. It is shown that using unrepresentative surface albedo at the ARM SGP Central Facility (CF) site can lead to a significant discrepancy in the NIR spectral region, which underscores the importance of a correct specification of surface albedo values in modeling radiative transfer. To isolate the effect of the surface, only overcast uniform low-level single-layer clouds cases are considered. The next section describes the data and the model used in the study. Section 3 presents comparisons of downwelling spectral irradiance from the model and from observations. Section 4 discusses the inference of surface albedo from downwelling spectral transmittance. A summary of the study is presented in section 5.

2. Data and Methodology

[6] A combination of data sets collected at the CF in north-central Oklahoma from August 1997 to October 2000 was analyzed extensively for identifying single-layered, low-level, non-precipitating clouds. Such clouds are more suitable for radiative transfer modeling using the plane-parallel radiative transfer approach. Microphysical properties of water clouds may be modeled using Mie theory. The main data stream for selecting cloud cases include broadband measurements of downward surface fluxes, cloud radar snapshots, Surface Meteorological Observing System (SMOS) measurements, and satellite images from the Visible and Infrared Scanner (VIRS) aboard the NASA Tropical Rainfall Measuring Mission (TRMM) platform. The first criterion for a measurement to be flagged as cloudy data is that the direct component of the surface solar broadband irradiance be less than 5 Wm^{-2}. Note that the surface broadband solar irradiance data used here were not the raw data available from the ARM archive, but data reprocessed at the Pacific Northwest National Laboratory following a complex procedure to assure the best quality [C. Long et al., private communication, 2001]. The raw fluxes acquired by the Solar Infrared Radiation Station (SIRS) and pre-1998 Broadband Shortwave Radiation Network (BSRN) systems were corrected for thermal offset errors [*Dutton et al.*, 2001], followed by an inter-comparison of simultaneous measure-

ments by different observation systems to screen out any anomalous data. In addition, satellite observed radiance fields, when available, were used to identify the morphology and phase (water/ice) of the cloud field in the vicinity of the CF. Hourly weather observations collected by on-site personnel provided additional useful information, such as the state of the ground conditions at the site. The final screening of cloud cases depended on the availability of high-resolution solar spectral irradiance data from the Rotating Shadowband Spectroradiometer (RSS). The RSS was developed at the Atmospheric Sciences Research Center of the State University of New York in Albany and has been operating at the ARM site since August 1997 [*Harrison et al.*, 1999]. It provides total-horizontal, diffuse-horizontal, and direct-normal spectral irradiance measurements in 1024 channels from 360 to 1050 nm at a variable resolution ranging from about 0.15 nm to 2 nm. Note that such high-resolution data were available after August 29, 1998; before then, the data had only 470 channels. The RSS data were calibrated with a precision of 1% by Langley analysis and linked to an absolute calibration standard using a portable Li-COR lamp. After analysis of the ARM data at the CF from August 1997 until October 2000, cloud cases observed on nineteen days encompassing all seasons fulfilled the rigid requirements and were subsequently studied.

[7] The latest version of the Moderate-Resolution Transmittance 4 (MODTRAN-4) radiative transfer code [*Anderson et al.*, 1999] was employed which incorporates a discrete ordinates (DISORT) radiative transfer model dealing with multiple scattering processes. Radiosonde soundings provided atmospheric profiles of pressure, temperature, and water vapor. Total column amounts of water vapor and liquid water were available from microwave radiometer (MWR) retrievals. Water vapor mixing ratio profiles were calculated from the humidity, pressure and temperature profiles and scaled to MWR retrievals. Satellite data from the Total Ozone Mapping Spectrometer provided ozone column amount. The MODTRAN-4 code has a built-in rural aerosol model and aerosol loading is specified by visibility either at 5 km or 23 km. Over the SGP, it is believed that a rural type of aerosol with a visibility of 20 km can reasonably represent average aerosol conditions. In any case, there were no column aerosol data under overcast conditions; the effect of aerosol under thick cloud cover is relatively minor. Initial values of surface albedo were obtained from the MultiFilter Rotating Shadowband Radiometer (MFRSR) system that measured upward and downward spectral irradiances at several discrete wavelengths (415, 500, 608, 664, 860, and 938 nm) 10 m above the ground at the CF site. MFRSR surface albedo data have been used in several ARM investigations, such as in a closure test of the clear-sky radiative transfer [*Mlawer et al.*, 2000]. Cloud top boundaries were determined using radar reflectivity observed by the millimeter-wave cloud radar deployed at the CF. A threshold method was used whereby the background noise level was subtracted from the calibrated power signal. The location of a cloud layer was determined at heights where the subtracted signal changed sign. Ceilometer observations were also used to validate the cloud base height. For those times of the year when insect contamination is greatest, determination of cloud top height from radar becomes difficult. In these cases, cloud top height was estimated from radiosonde soundings at the altitude where the relative humidity exceeds 94%, according to *Dong et al.* [2000].

[8] Once cloud boundaries were found, vertical profiles of liquid water content were derived. *Frisch et al.* [1995] proposed a relatively simple method for deriving the vertical liquid water content for stratus clouds, based on the knowledge of cloud boundaries, reflectivity Z (m^3) from cloud radar, and integrated liquid water path (LWP) retrieved from the MWR. It is given by

$$q_1 = 0.3\,\rho\, Z^{1/2} N^{1/2}, \tag{1}$$

where N (m^{-3}) is the number density of cloud droplets that is assumed to be constant with height, q_1 is the profile of liquid water at level l and ρ is the density of water in g/m^3. Integrating this expression over the vertical range of a cloud yields the liquid water path. Since the liquid water path is known, N can be computed as

$$N = \left\{ \mathrm{LWP} \Big/ \left[0.3\,\rho \int Z^{1/2} \mathrm{dl} \right] \right\}^2. \tag{2}$$

Substituting this into equation (1) gives

$$q_1 = \left(\rho\, \mathrm{LWP}\, Z^{1/2} \right) \Big/ \int Z^{1/2} \mathrm{dl}. \tag{3}$$

Liquid water content profiles for low-level water clouds can be determined from this expression.

[9] Cloud microphysical properties for a particular cloud case were obtained by first determining a proper extinction coefficient, β, through an iterative process. Starting with an initial guess for β, modeled and RSS-observed surface fluxes at 500 nm were compared and depending on the sign of the relative difference, β was modified accordingly. This iterative process (i.e., change β, calculate flux, compare to RSS flux, and effect appropriate change to β) continued until agreement was achieved between the simulated and RSS-observed downward surface fluxes. Effective radius, R_{eff}, was then calculated using this final β and the liquid water path, LWP, following the relation

$$R_{\mathrm{eff}} = 1.5\,\mathrm{LWP}/\tau, \tag{4}$$

where τ is cloud optical depth, i.e., β multiplied by the cloud layer thickness. For the cases considered here, effective radii generally varied from about 5 to 11 μm, consistent with typical values for stratiform clouds estimated for the same region by *Dong et al.* [2000]. The cases selected are summarized in Table 1, which encompass all seasons with more cases in the fall and winter than in the summer and spring.

3. Comparison Between Observed and Modeled Spectral Irradiance

[10] With atmospheric and cloud parameters that were either directly observed or inferred from other measurements, downwelling spectral solar irradiances were com-

Table 1. A Summary of the Overcast Cloud Cases Selected for the Study and Their Mean Attributes

Date	Time, UTC	Column Amount, cm: Water Vapor	Liquid Water	O_3	Cloud Position, km	τ	R_{eff}, μm
971019	17:30	1.6	0.007	0.34	0.57–0.85	17.9	5.9
	17:35	1.6	0.007	0.34	0.61–0.85	15.8	6.8
	17:40	1.6	0.007	0.34	0.58–0.85	17.4	5.8
	17:45	1.6	0.007	0.34	0.59–0.85	15.7	6.6
	17:50	1.6	0.008	0.34	0.58–0.85	16.5	7.2
	17:55	1.6	0.008	0.34	0.60–0.86	21.1	5.7
	18:00	1.6	0.009	0.34	0.61–0.86	20.8	6.6
	19:00	1.6	0.015	0.34	0.55–0.94	36.4	6.0
971020	14:30	2.3	0.027	0.29	0.84–1.40	36.8	10.9
971026	21:00	1.2	0.007	0.34	0.77–1.02	14.4	7.6
971106	15:30	0.7	0.001	0.29	0.64–0.78	7.8	2.6
971210	20:30	0.9	0.008	0.34	0.76–1.20	22.9	5.2
971212	18:00	0.4	0.005	0.34	0.73–0.97	18.6	3.8
971222	17:30	1.4	0.002	0.34	0.58–1.00	10.0	2.9
971225	19:30	0.9	0.027	0.36	0.62–1.27	54.3	7.6
	19:40	0.9	0.013	0.36	0.87–1.27	35.2	5.7
	19:50	0.9	0.015	0.36	0.83–1.23	29.7	7.8
980113	20:30	1.0	0.012	0.33	0.45–1.00	27.7	6.6
980208	20:55	1.4	0.005	0.33	1.50–1.80	7.1	10.1
980330	18:30	2.8	0.008	0.34	0.34–0.75	12.5	10.0
980403	18:39	1.4	0.034	0.38	1.00–1.50	55.1	9.3
980429	20:30	1.9	0.043	0.40	0.82–1.42	65.0	10.0
980604	14:15	4.2	0.009	0.31	0.60–1.58	19.0	4.3
980805	17:31	4.1	0.019	0.33	1.49–1.88	25.9	9.1
200213	17:00	1.2	0.011	0.34	0.32–0.69	34.2	4.7
200303	18:15	1.2	0.018	0.34	0.50–0.96	25.9	10.4
200314	18:30	2.1	0.062	0.37	0.96–2.00	65.8	6.5
200315	17:00	2.0	0.012	0.33	0.40–0.72	24.6	7.1

puted and compared to RSS data. Figure 1 presents some sample results of the comparisons on one day for each season: 3 March 2000 for spring, 4 June 1998 for summer, 19 October 1997 for fall, and 22 December 1997 for winter. Due to tuning of the cloud properties at 500 nm, it is not surprising to see good agreement over the visible region. In the NIR region (>0.7 μm), varying degrees of disagreement were noticed. There exists a good agreement in the fall where modeled spectral transmittance matches very well with observations in terms of both magnitude and spectral variation. However, differences in other cases are so significant that they cast a reasonable doubt on the modeling of radiative transfer during these seasons.

[11] Noting the strong seasonal trend and the abrupt jump of the discrepancy near the chlorophyll absorption band at 700 nm, we postulate that it is an artifact resulting from inadequate representation of the surface spectral albedo in the radiative transfer model. This hypothesis is sound, given that the MFRSR instrument measuring surface albedo is mounted 10 m above a small area of tall wild grass that is surrounded by vast areas of agricultural fields and pastures. Figure 2 presents four clear-sky Landsat Thematic Mapper (TM) scenes covering the four seasons that shows the spatial and seasonal patterns and supports the comparison results. In winter through early spring, the tall grass becomes brown with a relatively low albedo in the NIR, whereas the surrounding area is dominated by dark green vegetation (wheat fields and pastures) that has much higher NIR albedo. Radiative interaction between the cloud layer

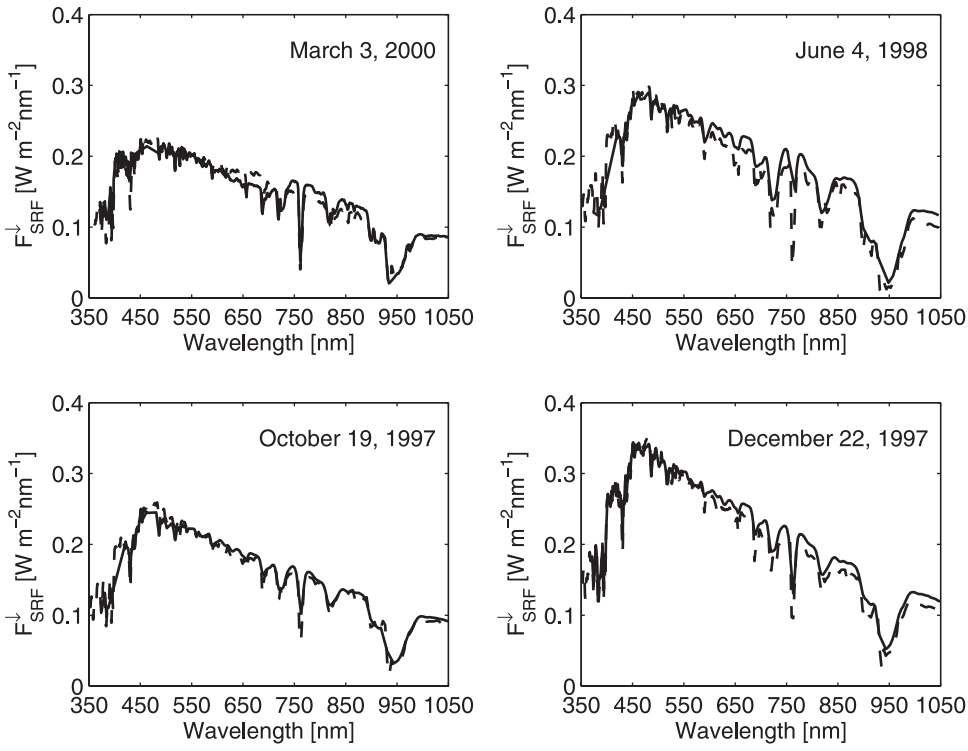

Figure 1. Comparisons between observed (solid-curve) and modeled (dashed-curve) downward surface fluxes as a function of wavelength for four cases in spring (top left), summer (top right), autumn (bottom left) and winter (bottom right). Model fluxes were computed by the MODTRAN-4 code using various observational input data including the MFRSR surface albedos.

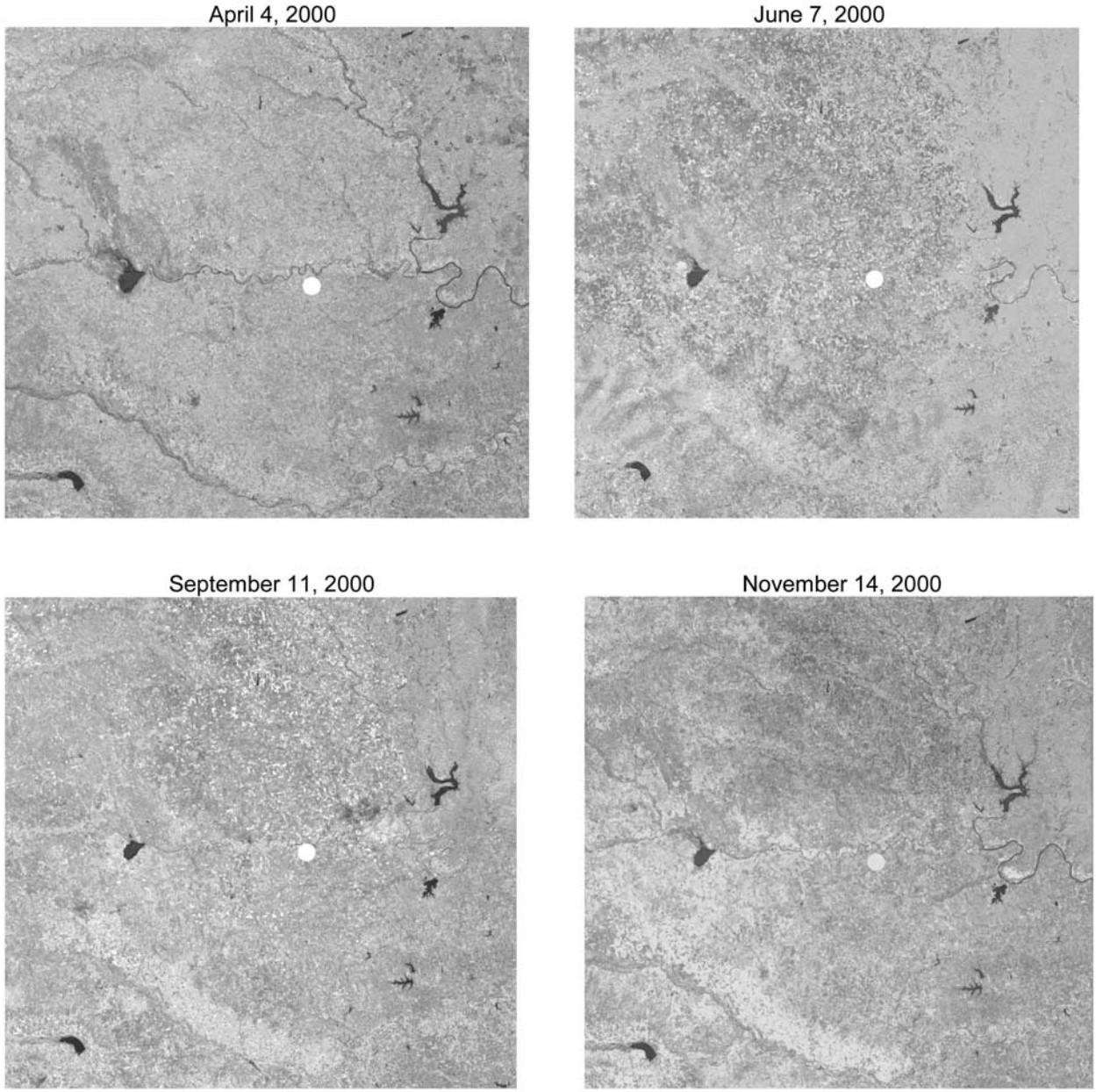

Figure 2. Clear-sky Landsat Thematic Mapper (TM) scenes acquired in four seasons around the CART Central Facility (CF) as marked by the white spot. See color version of this figure at back of this issue.

and the surface results in an effective surface albedo that echoes a much larger area than that exposed to the MFRSR. In this case, the MFRSR-observed value tends to underestimate the areal-mean albedo. The underestimated surface albedo gives rise to underestimated downwelling irradiance derived from model. In the summer, especially around June, changes in land cover over the region are more dramatic and complex because of the ripening and harvesting of wheat. Several fields of wheat in the vicinity of the CF exert significant impact on radiative processes in the area. Depending on their presence/disappearance they would contribute to major changes in surface albedo. The comparison suggests that by June 4, 1998, the immediate area surrounding the CF is still less green relative to a larger area sensitive to the downwelling radiation measurements, due presumably to the harvesting of wheat. In the fall, agricultural land is strewn with straw whose albedo is similar to dead grass so the entire region shows the least spatial contrast in surface reflectance.

[12] To test the hypothesis quantitatively, field measurements of spectral surface albedo over an area of about 50 $\times$ 50 km^2 surrounding the CF were taken during March 11–12, 2000. This period not only coincided with the ARESE II Intensive Observation Period (IOP), but also represents the best time of the year when surface inhomogeneity exhibits its most distinct spectral features. Broadly speaking, typical land cover types include alfalfa, bare soil, bare soil with dry corn stalks or wheat stubble, grazed and ungrazed pasture,

Figure 3. Photos showing some typical land cover types around the CF, and the S2000/PC2000 spectrometer deployed in the field campaign. The photos were taken on March 11–12, 2000. See color version of this figure at back of this issue.

green wheat, ploughed field, and bush. Figure 3 shows photos of some of the common land cover types observed in the region and taken during our field campaign. Note that the photo of short dry grass was shot beneath the MFRSR tower at the CF, which is a distinct surface land type relative to the surrounding wheat field. A portable spectrometer, manufactured by Ocean Optics Inc (model S2000/PC2000), and mounted on a tripod is also shown. Before each measurement was taken, the device was carefully aligned to assure its position and orientation. It provides cosine-corrected spectral irradiance from 188 nm to 867 nm at a resolution of 0.33 nm (2048 channels) by a fiber optic probe that collects photons at 180° (the entire upper hemisphere), thus eliminating optical interface problems associated with

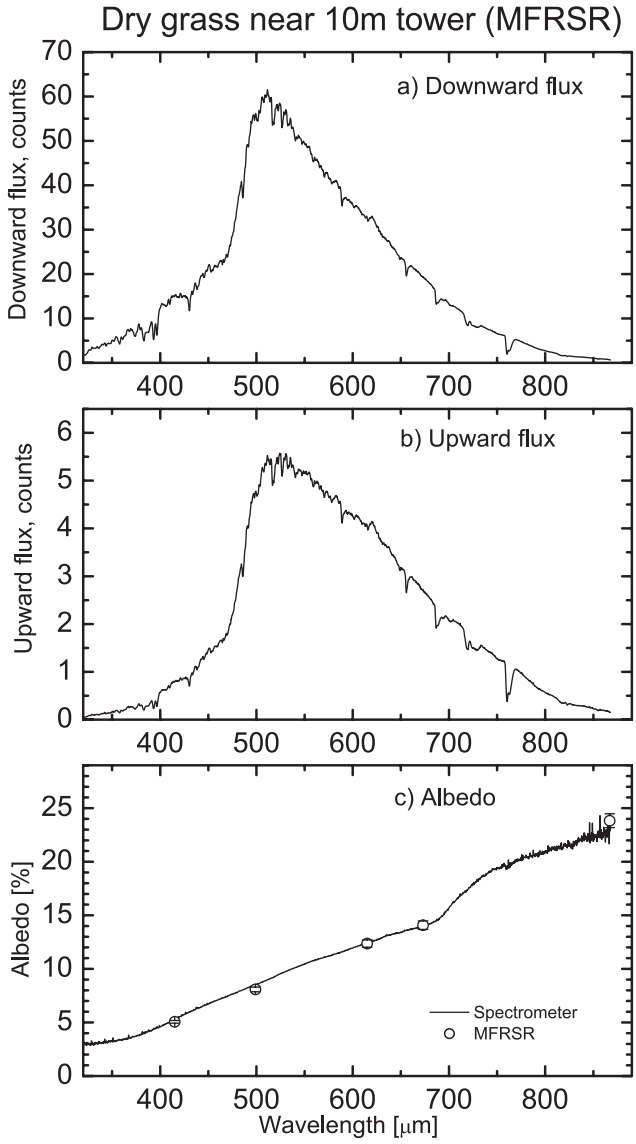

Figure 4. Spectral downward and upward fluxes and albedos measured with a S2000/PC2000 spectrometer on March 11, 2000, at the CF near the MFRSR 10-m tower. Open circles and error bars are synchronous MFRSR measurements averaged over ±30-min intervals centered at the acquisition time of spectrometer data.

the light collection sampling geometry inherent to other sampling devices. Measurements below 320 nm are too noisy to be of any use.

[13] Downward and upward measurements were taken nearly simultaneously (a couple of minutes apart) under clear sky conditions in order to compute their ratio. The estimated surface spectral albedo (ratio of instrument readings obtained in downfacing and upfacing positions) is thus invulnerable to calibration uncertainty. Since no reliable wavelength dependent calibration information for the spectrometer grating array was available, the absolute values were not employed in the study. A comparison against site-by-site measurements made by the calibrated MFRSR data attests to the quality of our measurements of spectral albedo, as shown in Figure 4. MFRSR data are averaged over ±30 minutes around the spectrometer measurements. The averaged MFRSR values and their standard deviation are shown in Figure 4. Using the device, we acquired many samples of surface albedo spectra collected over an area of 50×50 km^2 around the CF. Some dominant surface types such as winter wheat and pasture were sampled at varying local times to account for the dependence on the solar zenith angle. The latitude and longitude of each observation site were recorded by a hand-held civilian Global Position System (GPS). The geo-location is needed for mapping surface spectral albedo and computation of the solar zenith angle.

[14] Figure 5 is a synthetic plot of spectral surface albedos for numerous typical land cover types found in the region. Note that some of the curves represent single sets of observations, while others are averages of multiple data sets collected over the same or similar targets. It is seen that different land cover types found near the CF have very distinct albedo spectra. The largest differences occur in the NIR region where albedo for dark green vegetation like wheat reaches more than 50%, while bare ground has an albedo less than 20%. Differences in visible albedo are also discernable, particularly in relative values, with the highest and lowest visible albedos differing by a factor of 4. The diverse land cover types and distinct spectral albedos pose major challenges in simulating the radiative interaction between the atmosphere/cloud and the surface, requiring detailed mapping of surface spectral albedo over the region.

[15] Preliminary mapping of surface spectral albedo during one spring (2000) was achieved by linking the field measurements of surface spectral albedos with a land cover classification map derived from Landsat TM scenes by the U.S. Department of Agriculture's Agricultural Research Service (USDA-ARS) Hydrology and Remote Sensing Lab which conducted a field campaign known as the SGP Hydrology 1999 Campaign (available at http://hydrolab.arsusda.gov/sgp99/). The campaign made a special effort to classify land cover types over the SGP area. The classification was carried out by applying a supervised scheme to a series of cloud-free Landsat TM scenes from Landsat-5 (March 9, May 12, and July 15) and Landsat-7 (July 7 and July 23) in 1999. The nominal resolution of the data is 30 m. The classification scheme was developed with the aid of ground survey data collected from July 7–July 22, 1999. The ground survey data initially identified 44 different land cover categories that were then regrouped into 15 types. The distribution of the classified land cover is shown in Figure 6. Note that the area is predominately covered by wheat fields (designated as wheat stubble after being harvested), followed by pastures. While a lack of comprehensive ground-truth information prevents us from conducting a rigorous evaluation of the classification results, a cursory comparison with what we saw during our campaign in March 2000 lends certain confidence on the classification. Some local differences do exist due to multiyear shifts in agricultural practice that generally take place every 4 or 5 years (personal communication with local farmers). To remedy the problem, adjustments were made according to the greenness deduced from the TM scenes acquired in 2000. The adjustment is especially needed for distinguishing between wheat, bare soil with wheat stubble, and ploughed field. After refining the classification, each land cover type was assigned a particular observed albedo spectrum. Effective areal-mean

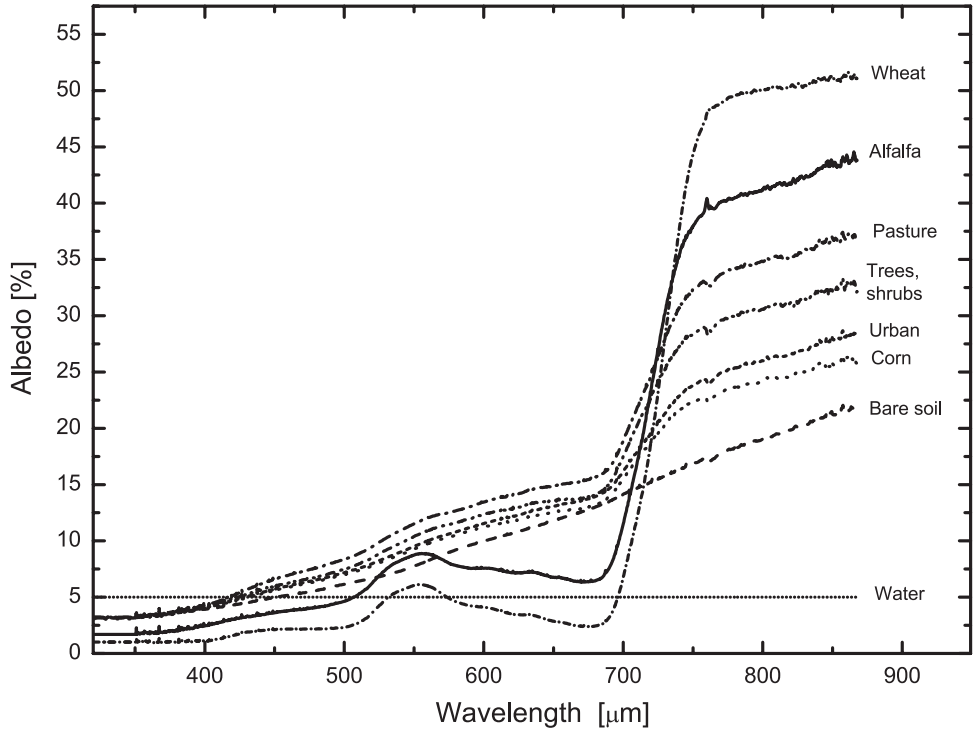

Figure 5. Spectral albedos for various basic surface types measured with the spectrometer on March 11–12, 2000.

spectral surface albedo was then obtained by integrating the spatial spectral albedo map over an area dictated by the cloud base height. The following formula was employed to compute the areal-mean albedo:

$$\alpha = \frac{\int \alpha(\Omega) d\Omega}{\int d\Omega} = \frac{\sum_{i,j \in allpixels} \alpha_{i,j} \frac{\Delta s_{i,j}}{L^2_{i,j}(h)} \cos\theta_{i,j}}{\sum_{i,j \in allpixels} \frac{\Delta s_{i,j}}{L^2_{i,j}(h)} \cos\theta_{i,j}} \quad (5)$$

where $\alpha_{i,j}$ is the albedo for pixel (i, j) derived from the field measurements and the land cover classification; $\Delta s_{i,j}$ is the area of a Landsat pixel, (30 m × 30 m) = 900 m^2; $L^2_{i,j}$ is the squared distance from an elevated virtual sensor to the pixel $(i, j) = h^2 + x_i^2 + y_j^2$; h is the altitude of the sensor and (x_i, y_j), the co-ordinates of the pixel relative to the CF; $\Delta s_{i,j}/L^2_{i,j}$ is equivalent to the derivative of the stereo angle; $\cos\theta_{i,j}$ is the viewing zenith angle for the pixel (i,j); $\Delta s_{i,j} \cos\theta_{i,j}/L^2_{i,j}$ is an element of the stereo angle (Ω) corresponding to a pixel area as seen by the sensor. The integration acts as if a spectrometer were located right beneath the cloud base. The resulting albedo spectrum data can thus be regarded as the observed albedo spectrum.

[16] Figure 7 presents a comparison of areal-mean albedo and point-based albedo measurements near the CF on March 3, 2000. Note that the areal-mean albedo varies with the cloud base height. In the NIR, it increases with cloud base height and the converse is true for the visible albedo. As the cloud height increases, the effective areal-mean albedo represents an enlarging area in which an increasing proportion of green vegetation (primarily winter wheat) is present. As the cloud base descends to the ground, the areal-mean albedo approaches the MFRSR point-based measurement, which is a clear trend visible in Figure 5. On March 3, 2000, the cloud base was in the neighborhood of 500 m. The discrepancies between the areal-mean albedo corresponding to 500 m and the point-based MFRSR measurements are substantial in the NIR. Significant differences also occur at longer wavelengths within the visible region. To investigate how much the discrepancy in surface albedo contributes to the discrepancy in downwelling spectral transmittance exhibited in Figure 1, radiative transfer simulations were re-run with the areal-mean albedo spectrum for 500 m. The new comparison (Figure 8) showed significantly improved agreement. It eliminates major discrepancies beyond 700 nm, and reduced those between 600 nm and 700 nm by half. Some improvement is also observed in the remaining spectra. This better agreement suggests a cautious treatment of surface albedo in any closure test of a radiative transfer model.

[17] The absence of a significant unexplained difference between observed and modeled RSS spectra is further reinforced by two more comparisons. One is the comparison of the broadband downward solar fluxes derived from the corrected BSRN and SIRS data and the broadband downward solar fluxes modeled with areal-mean surface albedo data together with other cloud and atmospheric input data as described in section 2. The top two plots of Figure 9 show the comparison for the nineteen days (more than nineteen points appear in the plot because multiple measurements were analyzed during some days). The top left plot shows transmittance at the surface and the top right plot, the corresponding downwelling surface fluxes in W m^{-2} (note that the correspondence of points is not one-to-one, owing to variable solar zenith angles). Again, a very good agreement is found, which is not totally expected from the

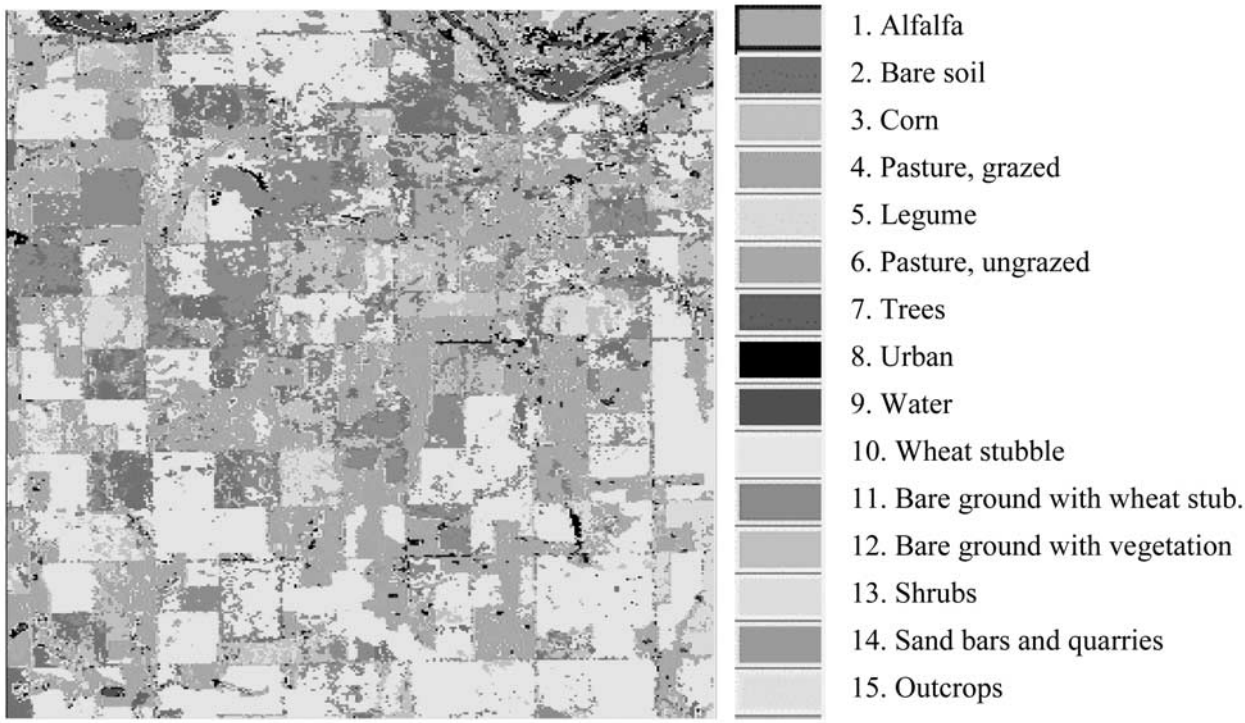

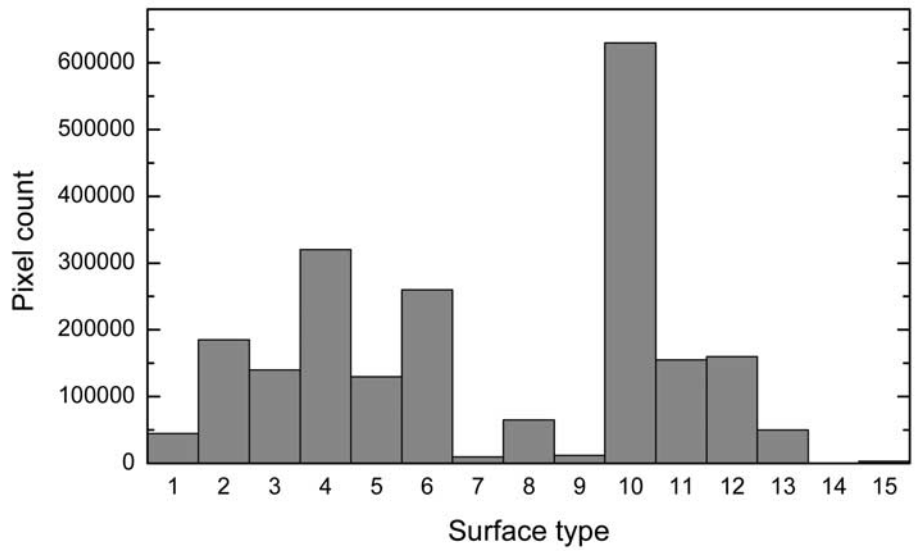

Figure 6. The spatial distribution (top image) and statistics (bottom plot) of surface types around the SGP CF site derived from Landsat TM data (courtesy of the website http://daac.gsfc.nasa.gov/CAMPAIGN_DOCS/SGP99/LC99.html). The size of the area shown is approximately 10 km × 10 km. The SGP CF is located at the center of the image. See color version of this figure at back of this issue.

spectral comparison shown in Figure 8 since the latter only covers a portion of the solar spectrum. Another comparison was made with reference to the TOA reflected radiances measured in the first two channels of the VIRS instrument, as shown in the bottom two plots of Figure 9 (left panel is for 0.63 μm and the right panel, for 1.6 μm). The comparison is not as conclusive as in the top panels, due to the very small number of samples. Nevertheless, it shows coherent results with Figure 8, namely, a better agreement in the NIR than at a longer wavelength of the visible spectrum.

4. A Method for Obtaining Effective Surface Areal-Mean Albedo

[18] If detailed and complete atmospheric and cloud data are available, spectral surface albedos may be inferred from

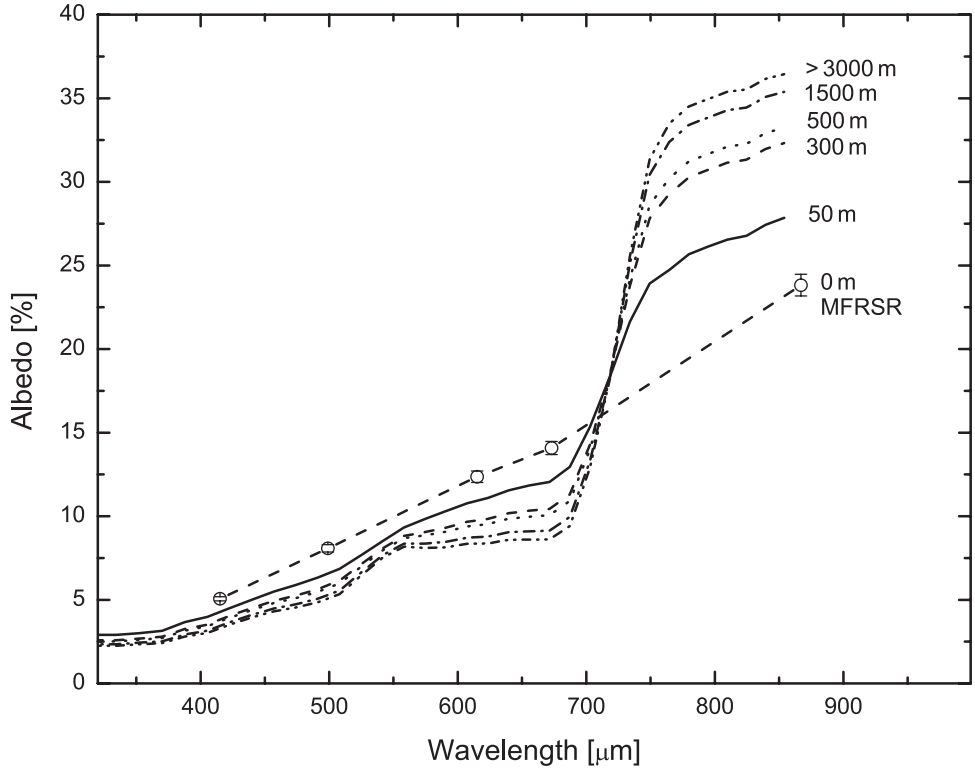

Figure 7. Areal-mean surface albedo at the CF derived from surface type data and the corresponding MFRSR-measured spectral albedos. Areal-mean albedos are computed as if a sensor were placed at various altitudes while MFRSR albedos were measured from a 10-m tower.

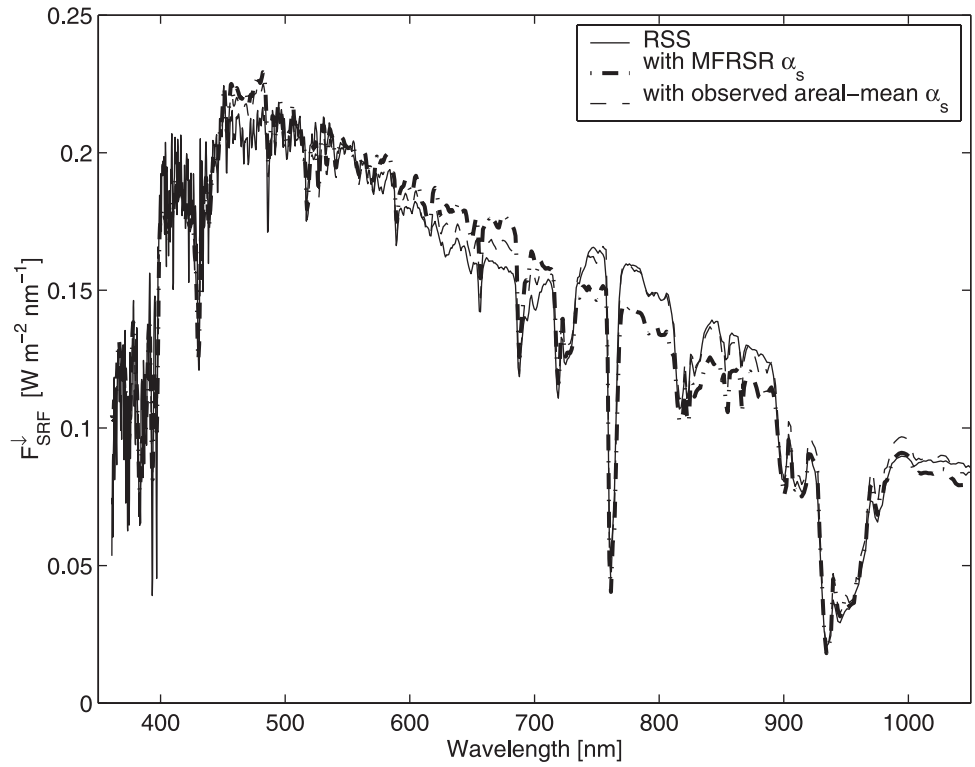

Figure 8. A comparison of solar transmittance at the surface between RSS measurements on March 3, 2000, and model simulations using two sets of surface albedo, point-measured MFRSR albedos and areal-mean albedos derived from field observations and land cover classification.

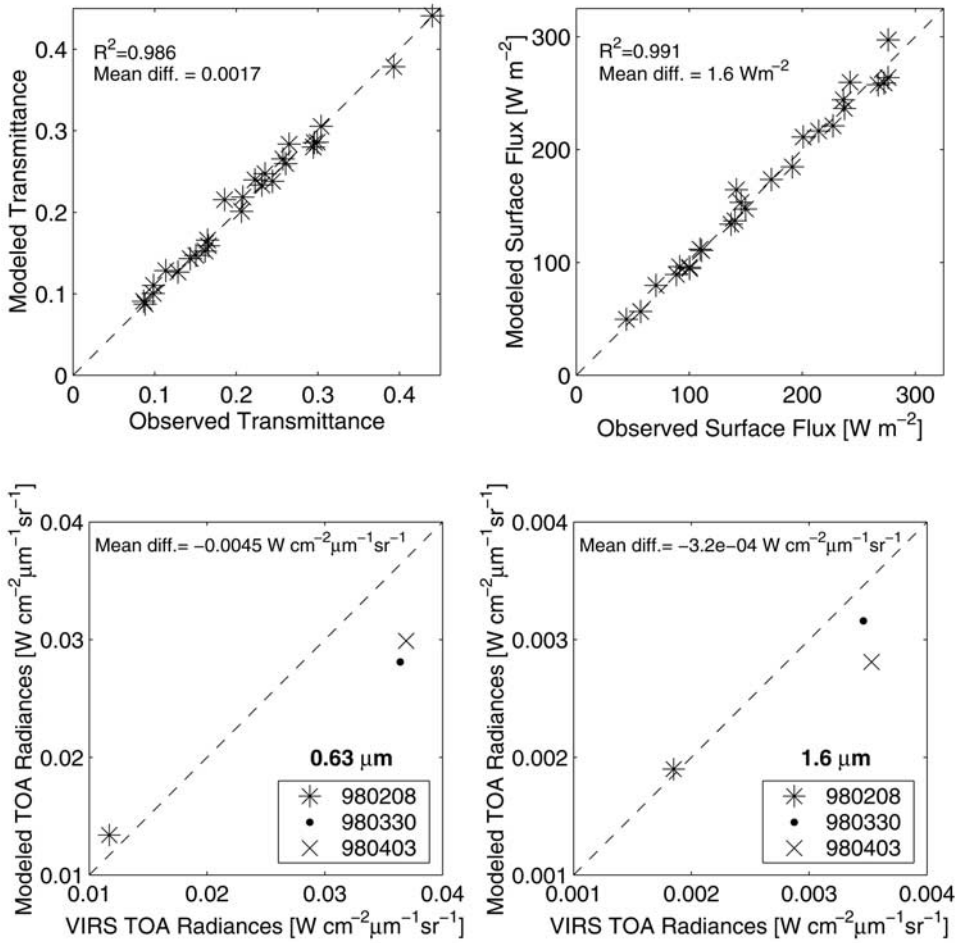

Figure 9. A comparison between modeled (using inferred areal-mean surface albedo) and observed (BSRN/SIRS) downwelling broadband shortwave transmittances (top left) and fluxes at the surface (top right). Bottom plots show a comparison of modeled and observed TOA radiances at 0.63 μm and 1.6 μm.

downwelling RSS measurements by tuning the surface albedo such that observed and modeled spectral fluxes match. To help understand the tuned albedo, a conceptual formulation is presented here.

[19] For a homogeneous cloud layer, which is assumed to be the case in this study, the downward solar flux $F_\lambda^\downarrow(r_0)$ at a location denoted by r_0 may be expressed as [see, e.g., *Barker et al.*, 2002]

$$F_\lambda^\downarrow(r_0) = F_{0\lambda}^\downarrow + \int_\Sigma dr\, \alpha_\lambda(r) F_\lambda^\downarrow(r) G_\lambda(r, r_0) \tag{6}$$

where $F_{0\lambda}^\downarrow(r_0)$ is the total downwelling irradiance at a point r_0 due to photons scattered by the atmosphere only, $\alpha_\lambda(r)$ is the local surface albedo and $G_\lambda(r, r_0)$ is a radiative Green's function describing the transfer of photons reflected from surface point r into downwelling photons at point r_0. Integration is performed over the entire surface domain, denoted by the Σ. Note that $F_{0\lambda}^\downarrow(r_0)$ and $G_\lambda(r,r_0)$ depend on atmospheric and cloud conditions only; they are completely independent of the surface reflective properties. The flux term $F_{0\lambda}^\downarrow(r_0)$ may be computed by the MODTRAN model, assuming a black surface.

[20] For homogeneous surfaces whose albedo is a constant $\alpha_{0\lambda}$ over the entire spatial domain, equation (6) is reduced to

$$F_\lambda^\downarrow(r_0) = \frac{F_{0\lambda}^\downarrow}{1 - \alpha_{0\lambda} S_\lambda} \tag{7}$$

where S_λ denotes the atmospheric spherical albedo (the proportion of radiation reflected by the atmosphere back to the surface) at wavelength λ given by

$$S_\lambda(r_0) = \int_\Sigma dr\, G_\lambda(r, r_0).$$

In the case of a homogeneous surface, S_λ is also constant and independent on position r_0. The denominator of equation (7) accounts for multiple scattering between the surface and the atmosphere.

[21] For inhomogeneous surfaces, radiative processes are more complex due to the interaction between the 2-D albedo field, the atmosphere and the cloud fields. One may define an effective areal-mean albedo and downwelling atmos-

pheric irradiance as a convolution of Green's function and surface albedo,

$$\overline{\alpha}_\lambda(r_0) = \frac{1}{S_\lambda}\int_\Sigma dr\,\alpha_\lambda(r)G_\lambda(r,r_0), \tag{8}$$

$$\overline{F}^\downarrow_\lambda(r_0) = \frac{\int_\Sigma dr\,\alpha_\lambda(r)F^\downarrow_\lambda(r)G_\lambda(r,r_0)}{\int_\Sigma dr\,\alpha_\lambda(r)G_\lambda(r,r_0)} \tag{9}$$

so that

$$F^\downarrow_\lambda(r_0) = F^\downarrow_{0\lambda} + \bar{\alpha}_\lambda(r_0)\overline{F}^\downarrow_\lambda(r_0)S_\lambda. \tag{10}$$

While the transformation of equation (6) into equation (10) does not constitute a mathematical solution, it reveals the effect of the atmospheric-surface interaction over an inhomogeneous field. With a knowledge of surface albedo distribution $\alpha_\lambda(r)$ and atmospheric and cloud conditions, the equations (8)–(10) could be solved numerically using a 2-D radiative transfer scheme. However, in this study, we employed the MODTRAN 1-D model to determine a bulk albedo $\hat{\alpha}_\lambda(r_0)$, which assures that the model-computed $F^\downarrow_\lambda(r_0)$ agrees with the RSS-measured $F^\downarrow_\lambda(r_0)$.

[22] It suggests a simple scheme to infer surface albedo $\hat{\alpha}_\lambda$ from measured downward flux $F^\downarrow_\lambda$. The albedo is estimated by attributing the discrepancy between RSS-observed and model-computed fluxes as shown in Figure 1 to the effect of an incorrect surface albedo, provided that the other input parameters are correct. The procedure begins with calculating spectral fluxes $F^\downarrow_{MFRSR,\lambda}$ using MFRSR-measured surface albedos as an initial guess; calculations are made at the wavelengths observed by the RSS. Since the MFRSR albedos are measured at six discrete wavelengths (415, 500, 608, 664, 860, and 938 nm), they were linearly interpolated to the RSS wavelengths. To bypass the computation of atmospheric spherical albedo S_λ, one can combine these computations with the computation of spectral flux $F^\downarrow_{0,\lambda}$ for a black surface ($\alpha_\lambda = 0$). The tuned albedo $\hat{\alpha}_\lambda$ can be determined as

$$\hat{\alpha}_\lambda = \alpha_{MFRSR,\lambda}\frac{F^\downarrow_\lambda - F^\downarrow_{0\lambda}}{F^\downarrow_{MFRSR,\lambda} - F^\downarrow_{0\lambda}}\frac{F^\downarrow_{MFRSR,\lambda}}{F^\downarrow_\lambda}. \tag{11}$$

The final result is a set of surface albedos $\hat{\alpha}_\lambda$, which when used as input into an atmospheric model such as MODTRAN-4, will yield downward fluxes at the surface matching the RSS observations.

[23] While the tuned albedo $\hat{\alpha}_\lambda(r_0)$ is not identical to that defined in equation (8), the two are very close. Indeed, they are related to each other through the expression

$$\overline{\alpha}_\lambda(r_0)\overline{F}^\downarrow_\lambda(r_0) = \hat{\alpha}_\lambda(r_0)F^\downarrow_\lambda(r_0). \tag{12}$$

Introducing the albedo difference $\delta\alpha_\lambda(r_0) = \hat{\alpha}_\lambda(r_0) - \overline{\alpha}_\lambda(r_0)$ and the flux difference

$$\delta F_\lambda(r_0) = \overline{F}^\downarrow_\lambda(r_0) - F^\downarrow_\lambda(r_0), \tag{13}$$

one can derive an equation for the relative albedo difference ε as a function of the flux difference. This equation is expressed as

$$\varepsilon = \frac{\delta\alpha_\lambda(r_0)}{\overline{\alpha}_\lambda(r_0)} = \frac{\delta F_\lambda(r_0)}{F^\downarrow_\lambda(r_0)} = \frac{1}{\overline{\alpha}_\lambda(r_0)S_\lambda}\int_\Sigma dr\,\alpha_\lambda(r)\cdot\left[\frac{F^\downarrow_\lambda(r) - F^\downarrow_\lambda(r_0)}{F^\downarrow_\lambda(r_0)}\right]G_\lambda(r,r_0). \tag{14}$$

Without a detailed specification of the boundary condition, it is not possible to obtain exact estimates, though qualitatively, it is expected that the flux difference (13) and the relative difference (14) is quite small.

[24] Using the single-scattering approximation, one can express the flux difference through the areal-mean albedo as

$$F^\downarrow_\lambda(r_0) = F^\downarrow_{0\lambda} + \overline{\alpha}_\lambda(r_0)F^\downarrow_{0,\lambda}S_\lambda$$

$$\frac{\delta F^\downarrow_\lambda}{F^\downarrow_\lambda(r_0)} = \frac{[\overline{\alpha}_\lambda(r) - \overline{\alpha}_\lambda(r_0)]S_\lambda}{1 + \overline{\alpha}_\lambda(r_0)S_\lambda}. \tag{15}$$

Inserting (15) into (14) and introducing the notation

$$\Delta_\lambda = \max\left|\frac{\overline{\alpha}_\lambda(r) - \overline{\alpha}_\lambda(r_0)}{\overline{\alpha}_\lambda(r_0)}\right|,$$

one can derive a conservative estimate of the difference as

$$|\varepsilon| \le \frac{\overline{\alpha}_\lambda(r_0)S_\lambda}{1 + \overline{\alpha}_\lambda(r_0)S_\lambda}\Delta_\lambda.$$

It was estimated that the difference does not exceed 17% of the maximal albedo variability Δ_λ found in a region surrounding the CF. In fact, for thick overcast clouds as were selected for current investigation, radiative smoothing due to multiple scattering further diminishes the difference to much smaller values.

[25] This may explain the close match between the tuned spectral and observed albedos, which is found by comparing Figures 7 and 10 (top left) for March 3, 2000. Figure 10 presents MFRSR-observed and RSS-inferred surface spectral albedos for 4 days representing all four seasons. It is seen that the discrepancies between MFRSR point-based measurements and RSS-inferred areal-mean albedos are rather significant in most seasons except fall, and moderately large in winter. The inferred surface albedos on March 3, 2000, are very close to observed areal-mean values retrieved from assuming a cloud bottom height of 500 m (c.f. Figure 7). Note that the cloud bottom heights range from 430 m to 650 m on this day. Larger differences exist between 600–700 nm and around 950 nm. Comparisons between inferred areal-mean albedos and the point-based MFRSR measured visible and NIR albedos for all cases as depicted in Table 1 are shown in Figure 11. Overall, visible albedos agree reasonably well and NIR albedos have such large seasonal differences that they may not be suitable or need correction if used in radiative transfer modeling or regional climate modeling.

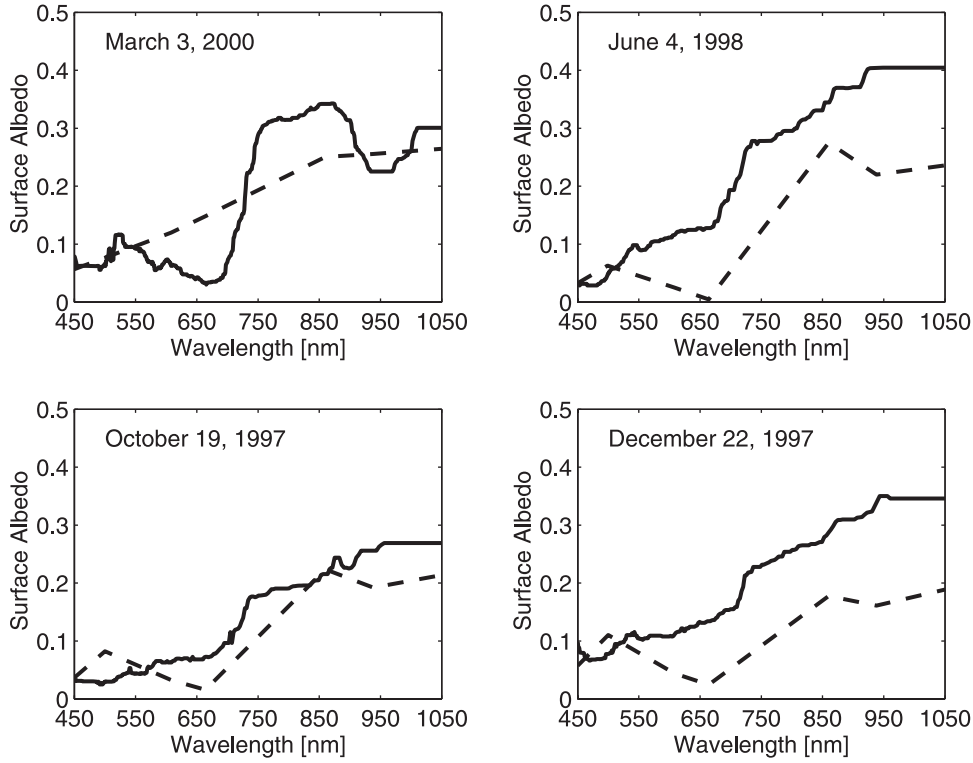

Figure 10. Estimated areal-mean surface albedo (solid lines) as a function of wavelength on one day in spring (top left), summer (top right), autumn (bottom left) and winter (bottom right), in comparison with MFRSR surface albedos (dashed lines).

[26] On the other hand, the above equations also underline the influence of uncertainties in atmospheric and cloud variables. Admittedly, the estimation of areal-mean albedo is not completely or always valid, since other input parameters also contain uncertainties. The reliability or degree of success of the estimation depends largely on how accurate other input variables are known, relative to the degree of surface inhomogeneity. As long as the impact of the other uncertainties on surface transmittance is less than that exerted by surface albedo, the attempt to estimate areal-mean albedo is worthwhile to make. Ideal cases for this exercise are overcast uniform single-layer non-precipitating water clouds with known microphysical properties as observed or inferred from the state-of-the-art ARM instruments. In such cases, the cloud essentially acts as a "mirror" which echoes the spectral signature of ground reflection over a large area. While the requirements for determining appropriate cloudy cases are stringent, it is not too formidable to develop a database that can delineate a reasonable intraannual variation of areal-mean albedo. In

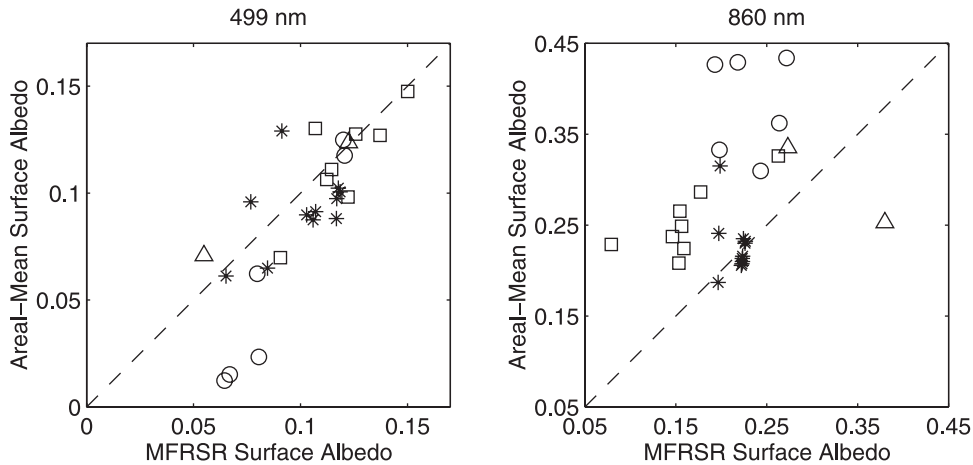

Figure 11. Comparisons between estimated areal-mean and MFRSR-measured surface albedos in the visible (499 nm) and near-IR (860 nm) for all identified overcast cases occurring in four seasons: spring (circles), autumn (stars), winter (squares), and summer (triangles).

general, changes in surface conditions are so gradual, except during a harvest period, that a limited number of cases spanning across a year may adequately depict the annual cycle of surface albedo changes.

5. Summary

[27] Radiative transfer modeling is essential to climate modeling and remote sensing. Inconsistencies between observations and modeling results has been reported. Ample measurements collected from the United States Department of Energy's Atmospheric Radiation Measurement (ARM) program, together with space-borne observations, provide an unprecedented opportunity to scrutinize any potential problems. In this study, we made extensive use of ARM data at the Central Facility to examine spectrally resolved solar radiative fluxes under overcast cloudy conditions. The study underscores the importance of taking into account surface inhomogeneity in a closure test of a radiative transfer model.

[28] Ground-based measurements used include radiosonde profiles of pressure, temperature and humidity, microwave radiometer retrievals of precipitable water vapor and liquid water total column amounts, cloud layer boundaries from laser ceilometer and cloud radar, spectral surface albedo from the MultiFilter Rotating Shadowband Radiometer (MFRSR), spectral fluxes from the Rotating Shadowband Spectroradiometer (RSS), best estimates of shortwave broadband fluxes from the Baseline Shortwave Radiation Network (BSRN) and Solar Infrared Radiation Station (SIRS) radiometers (corrected for thermal offset errors), and cloud parameters from the cloud radar and the microwave radiometer. Satellite data employed are Visible/Infrared Scanner (VIRS) data from the Tropical Rainfall Measuring Mission (TRMM) platform and thematic mapper (TM) data from Landsat 5 and 7.

[29] The measurements of atmospheric, cloud and surface variables for all relatively uniform cloud cases identified from August 1997 through to the late fall of 2000 were input into the MODTRAN-4 code. The model generated surface spectral and broadband fluxes and TOA fluxes. They were compared to both surface and satellite measurements. The model is capable of reproducing very well the general location and strength of the gaseous absorption lines, relative to observed spectra obtained by the RSS, but a larger disagreement is found over the near-infrared (NIR) region. The disagreement was attributed primarily to inadequate measurements of surface spectral albedo that are local values and do not adequately represent the larger surrounding area. Under overcast conditions, photons arriving at the RSS have survived multiple reflections between the surface and the cloud over an area determined by the height of the cloud. The effect was assessed quantitatively by taking ground measurements of the surface albedo spectra for all major land cover types found in the study region. In combination with a detailed land cover map classified with Landsat TM scenes, high-resolution surface spectral albedo data were obtained. Applying these data, along with other cloud and atmospheric input, to the MODTRAN-4 atmospheric radiation code yields model-simulated spectrally resolved and integrated fluxes in close agreement with observations at the surface and the top-of-the-atmosphere.

[30] The strong sensitivity of downward fluxes to the magnitude of the surface albedo under overcast conditions allows for the estimation of areal-mean surface spectral albedos from downwelling spectrometer measurements, provided that cloud and atmospheric parameters are known. Areal-mean surface albedo is otherwise a formidable task to measure using conventional means of observation. Taking advantage of this sensitivity and using all available ground and satellite observations, we first carefully selected ideal overcast cloud cases that were single-layered, low-level, non-precipitating, uniform water clouds. Input parameters obtained from measurements made at the Central Facility were applied to MODTRAN-4. Areal-mean surface spectral albedos were determined by tuning them to achieve good agreement between the resulting modeled surface spectral irradiance and observed surface spectral irradiance measured by the RSS. The retrieved albedos showed good agreement with independent estimations based on a 2-D albedo map derived from satellite and field measurements. Following this method, a sound seasonal areal-mean albedo dataset was developed for model and remote sensing studies.

[31] **Acknowledgments.** We are grateful to C. Long for providing the latest surface radiation data, W. Evans for lending us his Ocean Optics spectrometer for the field work, Tom Jackson for help with the Land Cover Classification data, R. Cahalan and G. Wen for making available some Landsat images, and L. Harrison and J. Michalsky as well as numerous other ARM personnel for their contributions to the acquisition of various ARM data sets used in the study. Helpful discussions with H. Barker are very much appreciated. The study was supported by the U.S. Department of Energy under its Atmospheric Radiation Measurement program with grant DE-FG02-01ER63166.

References

Anderson, G. P., et al., MODTRAN4: Radiative transfer modeling for remote sensing, in *Optics in Atmospheric Propagation and Adaptive Systems III*, edited by A. Kohnle and J. D. Gonglewski, *Proc. SPIE Int. Soc. Opt. Eng.*, *3866*, 2–10, 1999.

Arking, A., Bringing climate models into agreement with observations of atmospheric absorption, *J. Clim.*, *12*, 1589–1600, 1999.

Barker, H. W., and Z. Li, Interpreting shortwave albedo-transmittance plots: True or apparent anomalous absorption?, *Geophys. Res. Lett.*, *24*, 2023–2026, 1997.

Barker, H. W., A. Marshak, W. Szyrmer, J.-P. Blanchet, A. Trishchenko, and Z. Li, Inference of cloud optical depth from aircraft-based solar radiometric measurements, *J. Atmos. Sci.*, *59*, 2093–2111, 2002.

Dong, X., P. Minnis, T. P. Ackerman, E. E. Clothiaux, G. G. Mace, C. N. Long, and J. C. Liljegren, A 25-month database of stratus cloud properties generated from ground-based measurements at the Atmospheric Radiation Measurement Southern Great Plains Site, *J. Geophys. Res.*, *105*, 4529–4537, 2000.

Dutton, E. G., J. Michalsky, T. Stoffel, B. W. Forgan, J. Hickey, D. W. Nelson, T. L. Alberta, and I. Reda, Measurement of broadband diffuse solar irradiance using current commercial instrumentation with a correction for thermal offset errors, *J. Atmos. Oceanic Technol.*, *18*, 297–314, 2001.

Ellingson, R. G., The second ARM Enhanced Shortwave Experiment (ARESE II): Experiment description and initial results, paper presented at Chapman Conference on Atmospheric Absorption of Solar Radiation, AGU, Estes Park, Colo., 13–17 August 2001.

Frisch, A. S., C. W. Fairall, and J. B. Snider, Measurement of stratus cloud and drizzle parameters in ASTEX with a K_{α}-band doppler radar and a microwave radiometer, *J. Atmos. Sci.*, *52*, 2788–2799, 1995.

Gardiner, B. G., Solar radiation transmitted to the ground through cloud in relation to surface albedo, *J. Geophys. Res.*, *92*, 4010–4018, 1987.

Giver, L. P., C. Chackerian Jr., and P. Varanasi, Visible and near-infrared $H_2{}^{16}O$ line intensity corrections for HITRAN-96, *J. Quant. Spectrosc. Radiat. Transfer*, *66*, 101–105, 2000.

Harrison, L., M. Beauharnois, J. Berndt, P. Kiedron, J. J. Michalsky, and Q. Min, The rotating shadowband spectroradiometer (RSS) and SGP, *Geophys. Res. Lett.*, *26*, 1715–1718, 1999.

Li, Z., L. Moreau, and A. Arking, On solar energy disposition: A perspective from observation and modeling, *Bull. Am. Meteorol. Soc.*, *78*, 53–70, 1997.

Li, Z., A. Trishchenko, H. W. Barker, G. L. Stephens, and P. T. Partain, Analysis of Atmospheric Radiation Measurement (ARM) program's Enhanced Shortwave Experiment (ARESE) multiple data sets for studying cloud absorption, *J. Geophys. Res.*, *104*, 19,127–19,134, 1999.

Long, C., K. Younkin, and D. M. Powell, Analysis of the Dutton et al. IR loss correction technique applied to ARM diffuse SW measurements, paper presented at 11th ARM Science Team Meeting, Atmos. Radiat. Meas. Program, U.S. Dep. of Energy, Atlanta, Ga., 19–23 March 2001.

Marshak, A., W. Wiscombe, A. Davis, L. Oreopoulos, and R. F. Cahalan, On the removal of the effect of horizontal fluxes in two-aircraft measurements of cloud absorption, *Q. J. R. Meteorol. Soc.*, *125*, 2153–2170, 1999.

Marshak, A., Y. Knyazikhin, A. Davis, W. Wiscombe, and P. Pilewskie, Cloud-vegetation interaction: Use of normalized difference cloud index for estimation of cloud optical thickness, *Geophys. Res. Lett.*, *27*, 1695–1698, 2000.

Mlawer, E. J., P. D. Brown, S. A. Clough, L. Harrison, J. Michalsky, P. W. Kiedron, and T. Shippert, Comparison of spectral direct and diffuse solar irradiance measurements and calculations for cloud-free conditions, *Geophys. Res. Lett.*, *27*, 2653–2656, 2000.

O'Hirok, W., C. Gautier, and P. Ricchiazzi, Spectral signature of column solar radiation absorption during the Atmospheric Radiation Measurement Enhanced Shortwave Experiment (ARESE), *J. Geophys. Res.*, *105*, 17,471–17,480, 2000.

Pyatnenkov, B. A., Influence of albedo on total radiation income in the Arctic, *Tr. Arkt. Antarkt. Nauchno Issled. Inst.*, *217*, 157–173, 1959.

Rossow, W. B., C. Delo, and B. Cairns, Implications of the observed mesoscale variations of clouds for the Earth's radiation budget, *J. Clim.*, *15*, 557–585, 2002.

Stephens, G. L., and S.-C. Tsay, On the cloud absorption anomaly, *Q. J. R. Meteorol. Soc.*, *116*, 671–704, 1990.

Trishchenko, A. P., Z. Li, F.-L. Chang, and H. Barker, Cloud optical depths and TOA fluxes: Comparison between satellite and surface retrievals from multiple platforms, *Geophys. Res. Lett.*, *28*, 979–982, 2001.

Wielicki, B. A., R. D. Cess, M. D. King, D. A. Randall, and E. F. Harrison, Mission to planet Earth: Role of clouds and radiation in climate, *Bull. Am. Meteorol. Soc.*, *76*, 2125–2153, 1995.

Wild, M., A. Ohmura, H. Gilgen, and E. Roeckner, Validation of general circulation model radiative transfer fluxes using surface observations, *J. Clim.*, *8*, 1309–1324, 1995.

M. C. Cribb and Z. Li, ESSIC and Department of Meteorology, 224 CSS Building, Room 2207, University of Maryland, College Park, MD 20742-2465, USA. (mcribb@essic.umd.edu; zli@atmos.umd.edu)

A. P. Trishchenko, Canada Center for Remote Sensing, 588 Booth Street, Ottawa, Ontario, Canada K1A0Y7. (trichtch@CCRS.NRCan.gc.ca)

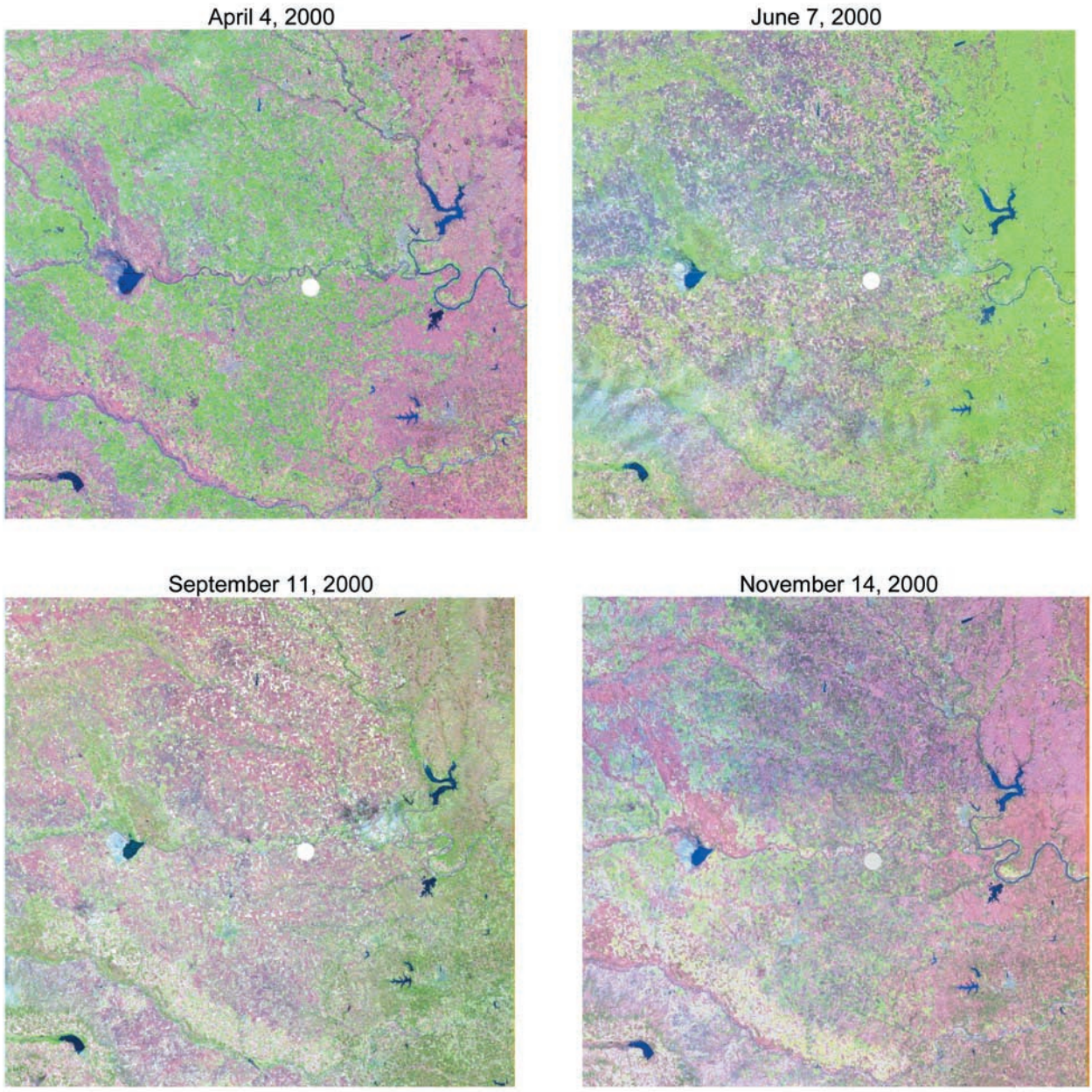

Figure 2. Clear-sky Landsat Thematic Mapper (TM) scenes acquired in four seasons around the CART Central Facility (CF) as marked by the white spot.

Figure 3. Photos showing some typical land cover types around the CF, and the S2000/PC2000 spectrometer deployed in the field campaign. The photos were taken on March 11–12, 2000.

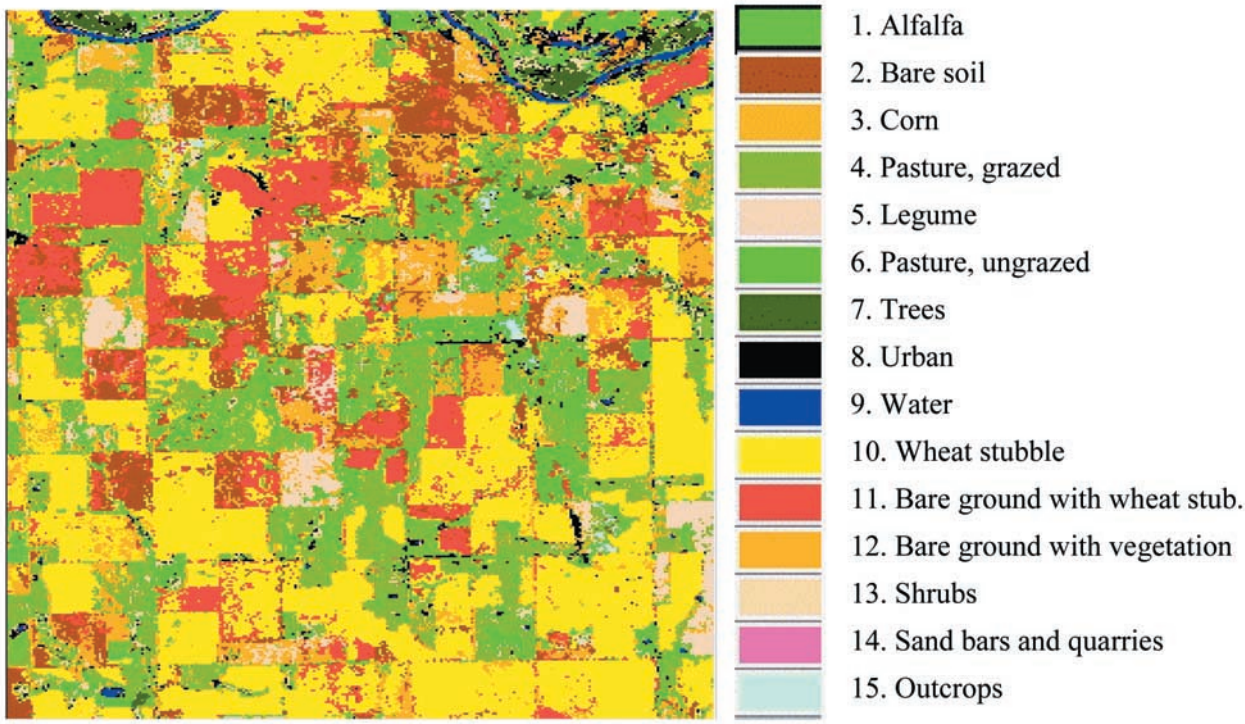

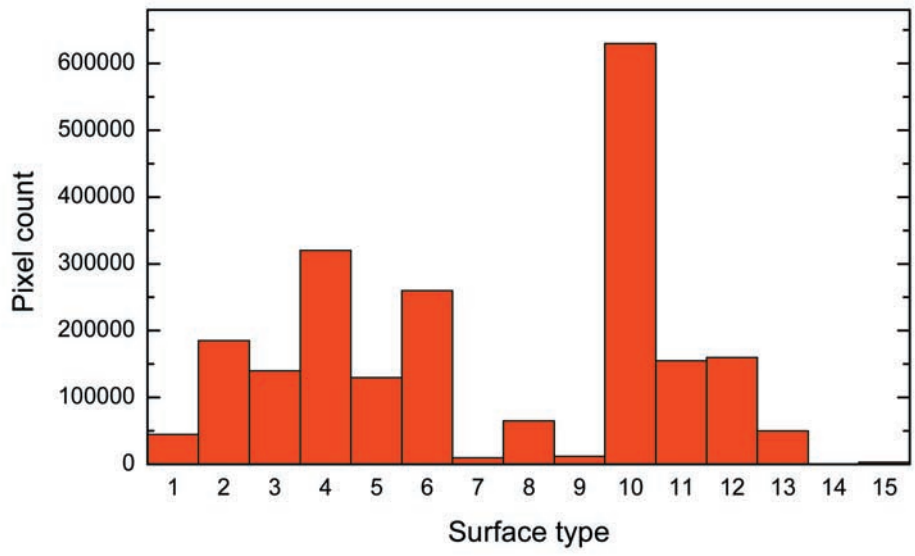

Figure 6. The spatial distribution (top image) and statistics (bottom plot) of surface types around the SGP CF site derived from Landsat TM data (courtesy of the website http://daac.gsfc.nasa.gov/CAMPAIGN_DOCS/SGP99/LC99.html). The size of the area shown is approximately 10 km × 10 km. The SGP CF is located at the center of the image.